Creep dynamics of elastic manifolds *via* exact transition pathways

Alejandro B. Kolton,[1, *] Alberto Rosso,[2, †] Thierry Giamarchi,[3, ‡] and Werner Krauth[4, §]

[1]*Centro Atómico Bariloche, 8400 S.C. de Bariloche, Argentina*
[2]*CNRS; Univ. Paris-Sud, LPTMS UMR 8626, Orsay Cedex, F-91405, France*
[3]*Université de Genève, DPMC, 24 Quai Ernest Ansermet, CH-1211 Genève 4, Switzerland*
[4]*CNRS-LPS*
Ecole Normale Supérieure, 24 rue Lhomond, 75231 Paris Cedex 05, France

We study the steady state of driven elastic strings in disordered media below the depinning threshold. In the low-temperature limit, for a fixed sample, the steady state is dominated by a single configuration, which we determine exactly from the transition pathways between metastable states. We obtain the dynamical phase diagram in this limit. At variance with a thermodynamic phase transition, the depinning transition is not associated with a divergent length scale of the steady state below threshold, but only of the transient dynamics. We discuss the distribution of barrier heights, and check the validity of the dynamic phase diagram at small but finite temperatures using Langevin simulations. The phase diagram continues to hold for broken statistical tilt symmetry. We point out the relevance of our results for experiments of creep motion in elastic interfaces.

I. INTRODUCTION

Disordered elastic systems are ubiquitous in nature. They appear as interfaces such as magnetic [1, 2, 3, 4] or ferroelectric [5, 6] domain walls, contact lines [7], fractures [8, 9], or as periodic structures, such as vortex lattices [10, 11], charge density waves [12] and Wigner crystals [13]. They all share the competition between elastic forces that tend to order the system and the microscopic disorder that seeks to distort its structure. This competition manifests itself in the static properties, leading to a roughness of the interfaces or a distortion of periodic order.

In addition, disorder leads to pinning and thus also affects the dynamical properties. Indeed practically all the above systems may be displaced through an external force (magnetic or electric field for magnetic or ferroelectric domain walls, current for vortices, etc.). The motion directly influences central observables of the system (e.g. magnetization for magnetic domain walls, voltage for vortices etc.).

The static properties of disordered elastic systems are now well understood. It has for example been established that interfaces (on which we will focus in this paper) become rough in the presence of disorder. The roughness is characterized by an exponent ζ_{eq}, which depends only on the universality class of the disorder, the dimension of the interface and the nature of the elastic forces. The dynamical properties are less well characterized. At zero temperature, disorder leads to the existence of a critical pinning force f_c, the depinning threshold, below which the interface is immobile, and above which steady-state motion sets in. The dynamics at finite temperature is

even more difficult to analyze than the zero-T behavior.

It has been particularly fruitful to consider the depinning transition as a regular critical phenomenon, with the velocity playing the role of an order parameter [14]. In this framework, the depinning transition appears linked to the existence of a correlation length ξ which diverges at the depinning transition, and to the presence of critical exponents, both for this length $\xi \sim (f - f_c)^{-\nu_{dep}}$ and for the velocity $v \sim (f - f_c)^\beta$. For zero temperature, the analogy of the dynamical depinning transition with equilibrium critical phenomena has been checked directly by numerical approaches and by analytical techniques such the functional renormalization group.

How to extend the analogy with critical phenomena to finite temperatures has not been completely evident. Measurements of the thermal rounding of the depinning transition, or observations of scaling for transient dynamics indicate that these ideas carry over to finite temperature [15, 16, 17]. However a direct study of the motion of such systems is very difficult for forces below the depinning forces, at finite temperature. Indeed in that case, the motion takes place by thermal activation over barriers, leading to extremely long activation times. This renders numerical techniques such as the molecular dynamics inefficient.

At finite temperature, the dynamics of a disordered system is very difficult to simulate, because of the high excitation barriers and the presence of thermal noise. Standard dynamical algorithms become very inefficient because the system is frozen in a local minimum. Advanced dynamical simulation methods, such as the BKL algorithm [18] and its variants cannot always be applied because the systems are in fact equilibrated on some length scale, leading to a futility problem [19, 20]: Not only does it take a long time to pass a barrier, but before doing so, the system will have undertaken a very large number of (futile) moves among local configurations.

This problem can often be overcome in statics, where we need not follow the very slow dynamics because observable averages are given by the Boltzmann weight

for each configuration. For this reason, many methods (transfer matrix, optimization algorithms, advanced Monte Carlo methods) allow one to characterize the thermodynamics of disordered elastic systems with an effort polynomial in the system size.

Similarly, although analytical techniques such as the functional renormalization group have been used with success to investigate the motion at finite temperatures, they lead to complicated equations that have been solved so far only for the 'creep' regime of very small forces $f \to 0$. Moreover, these techniques rely on an expansion around four spatial dimensions and are thus not very well adapted to tackle quantitatively realistic one- or two-dimensional interfaces.

In Ref [21] we introduced a novel numerical method which allows to follow the motion of an interface at finite temperature, without running into the above-mentioned difficulties. This algorithm was used to demonstrate that the analogy between the depinning and critical phenomena is incomplete. In fact, the steady-state motion lacks the divergent length for $f \to f_c$ from below. In the present paper, we discuss the algorithm in detail. We use it to study the various properties of an interface close to depinning. In addition to the questions of the steady-state motion and the corresponding divergent length scales and the roughness of the lines, we study the distribution of activation barriers during the motion. This is crucial since disordered elastic systems are glasses, with a priori divergent barriers. We also compare the results of our algorithm to molecular dynamics simulations, in order to check that taking the $T \to 0$ limit before the thermodynamic limit does not introduce artifacts.

The outline of this article is as follows: After a short review, in Section II, of the statics and the zero-temperature dynamics of disordered elastic systems, we outline in Section III the finite-temperature dynamical phase diagram obtained with our method. Section IV discusses the special properties of the low-temperature dynamics, which are used in the algorithm, and Section V contains a detailed description of our numerical results. A general discussion, including the prospects for experiments in Section VI, concludes this paper. Technical details of the algorithm and several mathematical proofs of key properties of the low-temperature dynamics are contained in Appendix A, whereas Appendix B resumes several properties of long-range elastic systems.

II.   BASIC NOTIONS

In order to render our paper self-contained, we review in the present section how the competition between disorder and elasticity manifests itself in the statics and the zero temperature dynamics of elastic manifolds. We stress the difference between equilibrium properties and the non-equilibrium steady-state behavior. Furthermore, we introduce the three 'reference states', the cornerstones of our analysis of the dynamical phase diagram
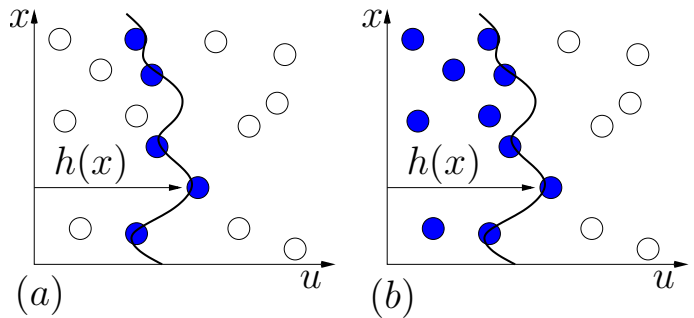

FIG. 1: (Color online) An elastic string $h(x)$ in a random medium. (a) For random-bond disorder (RB), its interaction with the impurities is local. (b) For random-field disorder (RF), the energy $E_{\mathrm{dis}}[h]$ depends on $V(u, x)$ for all $u < h$.
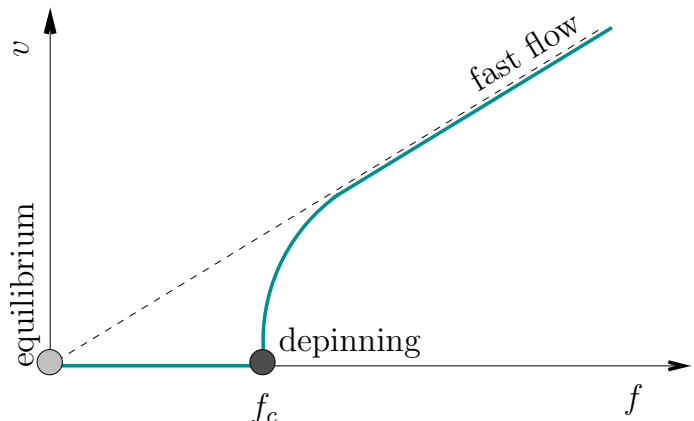

FIG. 2: (Color on line) Velocity–force characteristics of an elastic manifold at $T = 0$. The three self-affine reference states are: Equilibrium ($f = 0$); Depinning ($f = f_c$); Fast flow ($f \gg f_c$).

of Section III.

A.   Elastic manifolds

We consider a d-dimensional interface separating a $d + 1$-dimensional covering space into two regions. The interface is free of overhangs or loops, and may thus be described by a uni-valued displacement field $h(x)$. Fig. 1 shows an elastic string ($d = 1$) in a two-dimensional random medium, the case that we concentrate on in this paper.

The elastic energy $E_{\mathrm{el}}[h]$ is minimal for the flat manifold $h = $ const. For short-ranged elastic interactions, deviations from this configuration are often described by the harmonic energy

$$E_{\mathrm{el}}[h] = \frac{c}{2} \int d^d x \, (\partial_x h)^2 \tag{1}$$

(with an elastic coefficient c). This case applies to magnetic and ferroelectric domain walls as well as to vortex lattices and charge density waves.

	$f=0$ RB [26]	$f=0$ RF [27]	$f=f_c$ STS [28]	$f=f_c$ no STS [29]	$f\gg f_c$ EW	$f\gg f_c$ KPZ [30]
ζ	2/3	~ 1	~ 1.25	~ 0.633	1/2	1/2
z	∞	∞	~ 1.5	1	2	3/2
ν	Eq. (8)	Eq. (8)	Eq. (8)	~ 1.733	–	–

TABLE I: Zero-temperature critical exponents for an elastic string in the three self-affine reference states (equilibrium, depinning, fast flow).

Dipolar forces [5, 6, 22], contact lines for wetting [23], and also crack propagation [24] represent the class of manifolds with long-range elastic interactions. These systems are described by different harmonic forms (see Appendix B).

A second essential interaction is provided by the coupling of the manifold to disorder. Two types of disorder correlations have been much discussed in the literature: Random-bond (RB) disorder corresponds to impurities that locally attract or repel the interface (as for the wetting problem). In contrast, random-field (RF) disorder describes pinning energies which are affected by the impurities inside the entire region delimited by the interface (Fig. 1). This situation is encountered for example in magnetic systems when impurities modify the local magnetic field. The disorder potential E_{dis} generated by the impurities in these two cases is given by

$$E_{\text{dis}}[h] = \int d^d x \begin{cases} V(h(x), x) & \text{random bond} \\ \int_0^{h(x)} du V(u, x) & \text{random field,} \end{cases} \quad (2)$$

where for each value of x, the function $V(u)$ is a short-range-correlated Gaussian noise:

$$\overline{V(x,u)} = 0, \quad \overline{V(x,u)V(x',u')} = \delta^d(x-x')R(u-u') \quad (3)$$

where the over-bar stays for the average over all disorder realizations and $R(u)$ is rapidly decaying function.

A third interaction appears in the presence of an external force. With strong intrinsic dissipation, the following over-damped zero-temperature equation of motion applies:

$$\eta\partial_t h = -\frac{\delta(E_{\text{dis}} + E_{\text{el}})}{\delta h} + f = c\partial_x^2 h + F_{\text{dis}}(h, x) + f, \quad (4)$$

where η is a friction coefficient and F_{dis} is the pinning force. For small external force f, the manifold ends up pinned in a metastable state whereas it moves with finite velocity v at larger force. The moving phase is separated from the pinned regime by the critical force f_c [25].

B. Self-affine reference states ($T = 0$)

Three reference states are present in the velocity–force diagram at zero temperature (Fig. 2): the equilibrium (at $f = 0$), the depinning (at $f = f_c$), and the fast flow (at $f \gg f_c$). In these states, the manifold is spatially self-affine. This means that lengths x and displacements h above a small cut-off (set by the size of the corresponding Larkin domain [31]) can be rescaled as $x' = bx$ and $h' = b^\zeta h$ into a new interface $h'(x')$ which is statistically equivalent to $h(x)$. ζ is the state's characteristic roughness exponent. Even at finite temperature, manifolds can be analyzed in terms of these reference states, as we will discuss later.

1. Equilibrium ($f = 0$)

The large-scale properties of elastic manifolds at equilibrium are independent of temperature [26, 27, 32, 33, 34], because the disorder remains relevant. Indeed, sample-to-sample fluctuations of the ground-state energy grow with the system size L as $E_{\text{gs}} \sim L^\theta$ with a positive exponent θ.

The values of ζ_{eq} and θ depend on the dimension d, the range of the elastic interactions and on the type of disorder (RB or RF), but they are not independent: In a system of size L, the displacement h scales as $L^{\zeta_{\text{eq}}}$, and the short-range elastic energy as $L^{2\zeta_{\text{eq}}+d-2}$ (see Eq. (1)). At equilibrium, the elastic energy and the disorder contribution should scale in the same way. This implies the scaling relation

$$\theta = 2\zeta_{\text{eq}} + d - 2. \quad (5)$$

The motion is governed by the minimal energy barriers between metastable configurations. The barrier between configurations which differ over a size l is of order $U \sim l^\psi$ for large l, with a positive barrier exponent ψ. This power law is responsible for the logarithmically slow relaxation towards equilibrium [35, 36]. The relation $\psi = \theta$ is widely accepted [37] (see, however, [38], where $\psi = d/2$ is proposed).

2. Depinning ($f = f_c$)

At the depinning threshold $f = f_c^+$, the moving manifold is self-affine both in space and in time. This means that displacements $h(t) - h(0)$ on scales x and at time intervals $\sim t$ are statistically equivalent to displacements on scales $a^{\zeta_{\text{dep}}/z_{\text{dep}}}x$ at times $\sim at$ (here z_{dep} is the dynamic exponent). We note that in equilibrium the logarithmically slow dynamics prevents self-affinity in time.

Above the depinning threshold ($f \gtrsim f_c$), the velocity vanishes with a characteristic exponent, $v \sim (f - f_c)^\beta$, and the motion is characterized by avalanches of a divergent typical size ξ,

$$\xi \sim (f - f_c)^{-\nu_{\text{dep}}}. \quad (6)$$

In the language of critical phenomena, the velocity plays the role of the order parameter and the force the role of the control parameter [14].

The exponents β, ζ_{dep}, ν_{dep}, and z_{dep} are constrained by scaling relations [39, 40]. The velocity of the manifold is related to the characteristic time of an avalanche, $t \sim \xi^{z_{\text{dep}}}$, and to the distance the manifold advances during this time $\xi^{\zeta_{\text{dep}}}$, as $v \sim \xi^{\zeta_{\text{dep}} - z_{\text{dep}}}$. This yields a hyperscaling relation

$$\beta = \nu_{\text{dep}}(z_{\text{dep}} - \zeta_{\text{dep}}). \tag{7}$$

Depinning exponents depend on the dimension d of the manifold and on the range of the elastic interactions but they are independent of the type of disorder (RF or RB), merging the two equilibrium universality classes into one [41, 42].

Another scaling relation holds, both for depinning and equilibrium, if the equation of motion preserves the statistical tilt symmetry (STS) [41]. The tilt is a static force $\epsilon(x)$ with vanishing spatial average. If one adds a tilt to Eq. (4), and changes variables as $h(x,t) \to h(x,t) + \nabla^{-2}\epsilon(x)$ or, in Fourier space, $h(q,t) \to h(q,t) + q^{-2}\epsilon(q)$, the same equation of motion is recovered with a new realization of the same disorder. The statistical properties of the manifold are unchanged and the response function behaves like in the pure system $\overline{\partial h(q,t)/\partial \epsilon(q)} \sim q^{-2}$. Dimensional analysis of Eq. (6) implies that the force ϵ scales with the exponent $-1/\nu$. On the other hand, self-affine displacements h scale with the exponent ζ, so that:

$$\nu = \frac{1}{2-\zeta}. \tag{8}$$

Statistical tilt symmetry symmetry is violated by a non-harmonic elastic energy or by certain anisotropies of the random medium. This violation is relevant at depinning where a new universal behavior is observed [29, 43, 44]. A phenomenological mapping has been proposed between a one-dimensional string at the depinning transition and directed percolation [45, 46]. A concrete model belonging to this class contains elastic energies stronger than harmonic, for example

$$E_{el}[h] = \int d^d x \left[\frac{c}{2}(\partial_x h)^2 + c_4(\partial_x h)^4 \right], \tag{9}$$

with $c_4 > 0$ [43]. We note that the violation of statistical tilt symmetry changes the universality class at depinning, but not in equilibrium.

3. Fast flow $(f \gg f_c)$

In the fast-flow reference state, for $f \gg f_c$, the quenched pinning force reduces to an annealed stochastic noise [40] because in the co-moving frame, one has $F_{\text{dis}}(h,x) = F_{\text{dis}}(\delta h + vt, x) \sim F_{\text{dis}}(vt, x)$. For short-range correlated pinning force, the strength of the disorder plays the role of an effective temperature T_{eff}, since

$$\overline{F_{\text{dis}}(vt,x)F_{\text{dis}}(vt',x')} \sim \Delta(0)\delta(v(t-t'))\delta(x-x')$$

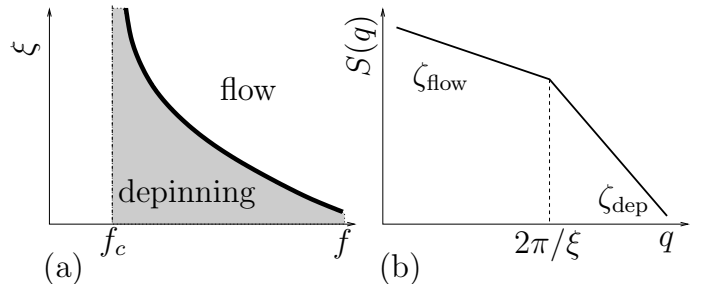$$= \frac{\Delta(0)}{v}\delta(t-t')\delta(x-x'),$$

FIG. 3: (a) Zero-temperature dynamical phase diagram. (b) Schematic structure factor for $f > f_c$. The correlation length ξ fixes the crossover between depinning and fast flow.

where $\Delta(0)$ measures the disorder strength. Since $dv/df \sim \eta^{-1}$ in this regime, it follows that $T_{\text{eff}} \sim \Delta(0)/(\eta v)$ from a generalized fluctuation–dissipation theorem. For the string, the fast-flow state corresponds to the random walk.

Critical exponents for the three self-affine reference states are summarized in Table I.

III. DYNAMIC PHASE DIAGRAM

At non-zero temperature, the manifold moves with finite velocity for all forces $f > 0$, and the long-time dynamics reaches a steady state. Possible steady states are contained in a dynamical phase diagram exhibiting, at different length scales, the three reference states of Section II. Above threshold, this diagram is well understood in terms of the analogy with second-order phase transitions.

The steady-state dynamics below threshold can be studied by means of our powerful algorithm which exploits the special properties of the dynamics (see Section IV). This algorithm yields a phase diagram which differs from the standard picture of a second-order phase transition.

A. Above threshold $(f > f_c)$

We first consider the region above the critical force where a steady state exists even at zero temperature. Here the analogy of the depinning transition with critical phenomena is well understood [14]: As in a thermodynamic second-order phase transition, the connected two-point correlation function of the order parameter is characterized by a correlation length which diverges at the critical point. The steady-state velocity is the order parameter of the depinning transition and its two-point correlation function,

$$\overline{\langle (v(x,t)-v)(v(0,t)-v) \rangle} \sim e^{-|x|/\xi}, \tag{10}$$

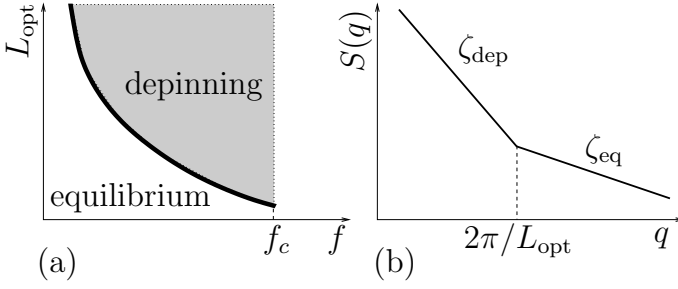indeed diverges for $f \to f_c^+$. Here, brackets stand for the thermodynamic (or steady-state) average. In practice,

FIG. 4: (a) Dynamical phase diagram for $f < f_c$ for vanishing temperature. (b) Schematic structure factor for $f < f_c$. The length L_{opt} fixes the crossover between equilibrium and depinning.
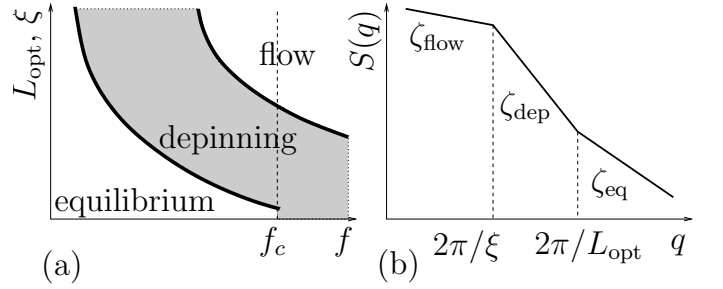

FIG. 5: (a) Dynamical phase diagram at finite temperature. (b) Schematic structure factor below f_c. The correlation length ξ fixes the crossover between depinning and fast flow, and the length L_{opt} the crossover between equilibrium and depinning.

this correlation function is not easily accessible because the steady-state velocities necessitate the long-time integration of the equation of motion [47].

The correlation length ξ separates two length scales in the manifold (see Fig. 3a): on scales smaller than ξ, the geometry of the interface is characterized by the exponents of the depinning reference state (the critical phase in the language of magnetic transitions). In contrast, on length scales larger than ξ, the interface is governed by the exponents of the fast-flow reference state (analogous to the ferromagnetic ordered phase of a magnetic transition). The length ξ can be measured [47] through the structure factor [48],

$$
\begin{aligned}
S(q) &= \overline{\left\langle \left| \frac{1}{L^{d/2}} \int d^d x \, h(x,t) \, e^{-iqx} \right|^2 \right\rangle} \\
&= \int d^d x \, e^{-iqx} \, \overline{\langle h(x,t)h(0,t) \rangle},
\end{aligned}
\tag{11}
$$

where the second equality makes use of spatial translation invariance. For inverse lengths q belonging to a self-affine regime with a single roughness exponent ζ, the structure factor takes the form

$$
S(q) \sim q^{-(d+2\zeta)}.
$$

The crossover between the depinning and the fast-flow regimes can be conveniently extracted from the change of slope of the structure factor $S(q)$ (see Fig. 3b).

B. Below the depinning threshold

Below the depinning threshold ($f < f_c$), at zero temperature, the manifold is permanently pinned. We first discuss the phase diagram in the limit of vanishing temperature, obtained with the methods of Section IV.

As in the regime above threshold, the structure factor allows us to access the self-affine regimes present in the interface. Our results from Section V are summarized in Fig. 4b. A crossover length, L_{opt}, associated to the maximal barrier encountered across the optimal path along the system, separates two roughness regimes: On

length scales smaller than L_{opt} the roughness of the interface is described by the equilibrium exponent ζ_{eq}, corresponding to the paramagnetic phase in the language of magnetic transitions. For distances bigger than L_{opt}, the roughness is described by depinning exponents (that is, the exponent of the critical phase). This is at variance with standard critical phenomenon, where the critical phase appears at large length scales only at the critical point. Our results are summarized in the phase diagram of Fig. 4a. Increasing the external force, L_{opt} decreases and when the depinning threshold is reached ($f \to f_c^-$), L_{opt} coincides with the Larkin length [31].

Our algorithm cannot access very small forces, but our results are compatible with predictions in the creep regime, that is, at low temperatures for $f \ll f_c$ [42, 48, 49, 50, 51]. In this regime, a phenomenological scaling argument suggests that the mean velocity is produced by activated jumps on a length scale which diverges in the equilibrium limit $f \to 0$ as $L_{\text{opt}} \sim f^{-\nu_{\text{eq}}}$. At this length, the typical energy barriers scale as

$$
U(f) \sim L_{\text{opt}}(f)^{\psi} \sim f^{-\mu},
\tag{12}
$$

where $\mu = \psi \nu_{\text{eq}}$ is the creep exponent. The velocity–force characteristics for small f is thus a stretched exponential. The functional renormalization group [42] predicts that on scales below L_{opt} the system is in equilibrium and that scales larger than L_{opt} are characterized by deterministic forward motion.

The structure factor at finite temperature is sketched in Fig. 5b. It presents three roughness regimes: for length scales smaller than L_{opt}, the interface is in equilibrium. Between L_{opt} and ξ, it is characterized by depinning exponents, and for larger lengths it is in the fast-flow regime. At finite temperatures, the two crossover lengths L_{opt} and $\xi \gg L_{\text{opt}}$ diverge as $f \to 0$ (see Fig. 5a). While $\xi(f,T)$ diverges for $T \to 0$ below the depinning threshold (see Fig. 3a), we find that $L_{\text{opt}}(f,T)$ saturates to a finite value $L_{\text{opt}}(f,T=0)$. The phase diagram of Fig. 5a exhibits the connection between depinning and equilibrium.
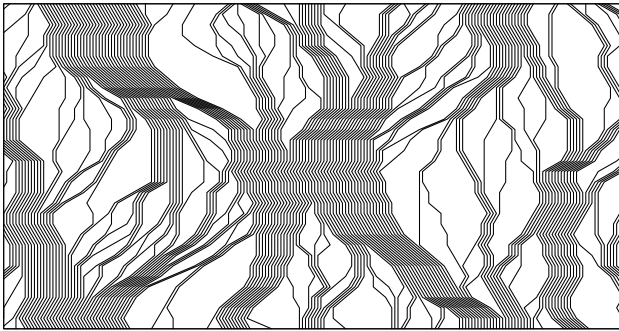
FIG. 6: Sequence of metastable configurations $\{\ldots, \alpha_k, \alpha_{k+1}, \ldots\}$ detected by our algorithm. For clarity, α_{k+1} is advanced by a small amount with respect to α_k.
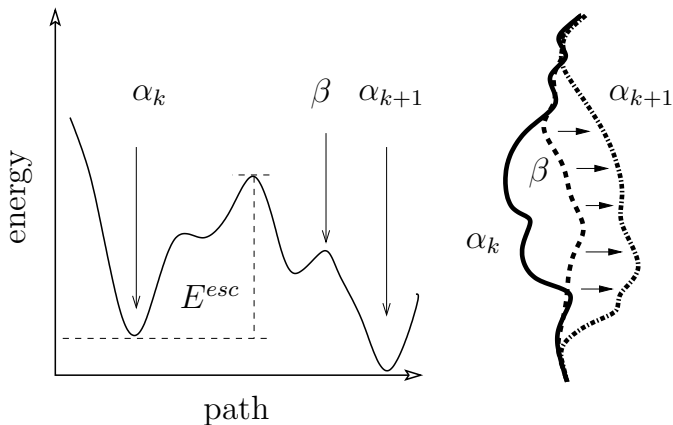

FIG. 8: Ground-state, critical and dominant configurations below f_c. An excitation of size L_{opt} escapes the system from the dominant configuration α. The configuration β relaxes to the metastable state γ *via* an avalanche of size L_{relax}.

FIG. 7: Escape path from a metastable configuration α_k *via* a configuration β that relaxes towards a new metastable configuration α_{k+1} of lower energy.

IV. $T \to 0$ DYNAMICS FOR FINITE SAMPLES

In this section, we discuss the detailed properties of the dynamics below threshold in the the zero-temperature limit for a finite sample. We call this the 'Arrhenius limit', because the time Δt to overcome an energy barrier U is governed by the Arrhenius formula $\Delta t \sim \exp[U/T]$. We show in the present section that in this limit the steady-state dynamics is characterized by a forward-moving sequence of metastable states of decreasing energy, which we are able to compute using the exact algorithm described in Appendix A. Moreover, below threshold, for each value of the external force, a unique dominant configuration is occupied with probability one, in the same way as for a finite system at equilibrium the occupation probability is entirely concentrated on the ground state.
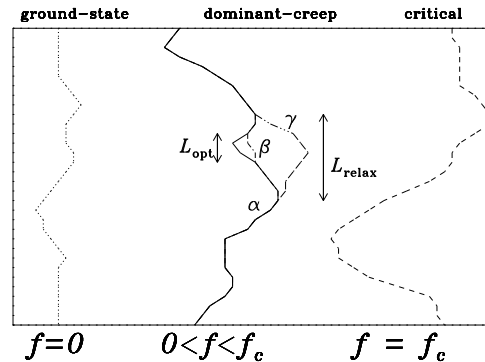
A.   Ordered sequence of metastable states

We first consider two metastable configurations α and γ at a fixed force f. A path $P_{\alpha \to \gamma}$ connecting α with γ is a sequence of configurations labeled with the time parameter t, as prescribed by the dynamics of the system, for example a discrete rule on a lattice, or a continuum Langevin prescription. The path barrier $P_{\alpha \to \gamma}$ between α and γ is given by

$$B[P_{\alpha \to \gamma}] = \max_t E[\alpha(t)] - E[\alpha], \tag{13}$$

and the barrier between the two metastable configurations, $B_{\alpha \to \gamma}$, is defined as the minimal path barrier over all paths connecting α with γ. In the Arrhenius limit, the escape time from a metastable state α is dominated by the minimal barrier ($E^{\text{esc.}}[\alpha]$) connecting α to a configuration with lower energy.

$$E^{\text{esc}}[\alpha] = \min_\gamma B_{\alpha \to \gamma}, \quad \text{with } E[\gamma] < E[\alpha].$$

The previous properties suggest the definition of a coarse-grained dynamics characterized by a sequence of metastable states, $\alpha_0, \alpha_1, ..., \alpha_k$ of decreasing energy connected by the minimal barriers E^{esc} (see Fig. 6 and Fig. 7). The transition from α_k to α_{k+1} is irreversible. This does not mean that from α_{k+1}, the microscopic dynamics cannot visit α_k again, but rather that escape paths from α_{k+1} towards a new configuration α_{k+2} with yet lower energy exist. In fact, as shown in Appendix A, the escape path can be implemented entirely with forward-moving steps, in the same way as for the zero-temperature motion relevant in the depinning problem [52, 53]. The same has been pointed out [54] for the Sinai model, where the effective dynamics involves forward moves only.

The sequence of metastable states has two remarkable properties. First, all configurations situated between configurations α_k and α_{k+1} have smaller escape energies

than the configuration α_k itself. Second, if in the backward direction, no metastable configuration exists which lowers the energy of α, then the coarse-grained dynamics starting from α is always forward-moving. These two properties (proved in Appendix A 2 and Appendix A 3) imply that the steady-state coarse-grained dynamics is always forward-directed. Furthermore, the metastable configuration characterized by the largest E_{esc} belongs to the sequence of configurations of the coarse-grained dynamics. This is the dominant configuration which, as discussed above, is occupied with probability one in the Arrhenius limit. Finally, the steady state of a sample with periodic boundary conditions describes a periodic trajectory of metastable configurations, which is independent of the initial configuration. These properties are analogous of the one-dimensional problem of a particle on a ring, which has been solved exactly [55, 56].

The details of the algorithm are given in Appendix A. It enumerates a complete set of dynamically relevant configurations. For driven manifolds, this approach is simpler than in general [19] because the excited configurations differ from the metastable configuration on a length scale L_{opt} which remains finite for $L \to \infty$. In addition, we can restrict ourselves to forward moves.

In Fig. 8 we compare the characteristic configurations of the low temperature dynamics: the dominant configuration, the ground-state, and the depinning critical configuration. These three configurations are the dominant states for $f = 0$, $0 < f < f_c$ and $f = f_c$, respectively. Our algorithm accesses also the configurations β and γ sketched in Fig. 8: configurations α and β differ on a length L_{opt}, and α and γ differ on a length L_{relax}. L_{opt} and L_{relax} are the characteristic dynamical lengths in the Arrhenius limit.

V. NUMERICAL RESULTS

Our algorithm determines, for each sample, the dominant configuration, the escape barrier E_{esc}, the size of the optimal thermal excitation L_{opt}, as well as the size of the deterministic avalanche L_{relax} (see Fig. 8). These results are also compared with the results obtained by other methods at finite and at zero temperature.

A. Analysis of the dominant configuration

We first consider the random-bond elastic string with statistical tilt symmetry. Complementing results of [21], we show in Fig. 9 the collapse of the structure factor of the dominant configuration at different forces, with all lengths rescaled by the disorder-averaged size of the thermal excitation, L_{opt}, which is obtained directly from the simulation. The remarkable quality of the collapse (which is free of adjustable parameters) is also due to the fact that the control parameter f/f_c, for each sample, is obtained with the sample-dependent critical force.
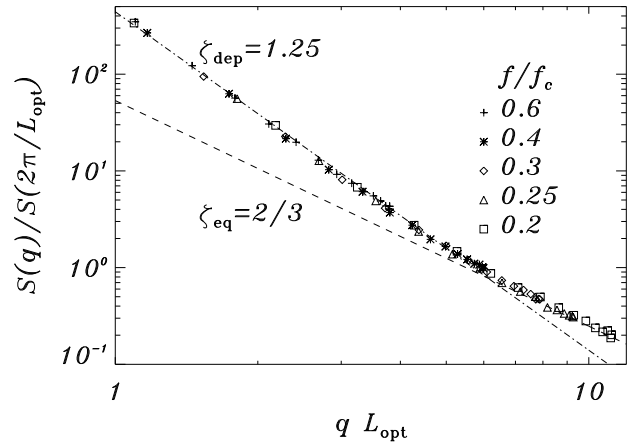

FIG. 9: Rescaled structure factor of the harmonic string in the Arrhenius limit (averaged over 1000 disorder realizations) for $L = 16, 32, 64, 128$.
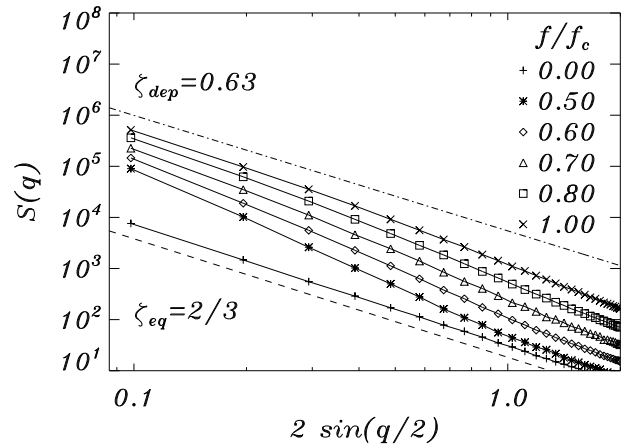

FIG. 10: Steady-state structure factor for a string with hard metric constraint in the Arrhenius limit (averaged over 10000 disorder realizations) for $L = M = 64$. Curves for different forces are shifted for clarity.

In Fig. 9, the change of regimes between the small-q region (governed by depinning) and the large q regime (dominated by equilibrium) is manifest. We note that L_{opt} characterizes the steady-state dynamics below f_c in the Arrhenius limit in the same way as ξ does above the depinning threshold [14, 47].

We now consider the model with a hard metric constraint, which violates STS. This case is particularly interesting because the equilibrium roughness exponents are identical, whereas the depinning exponents differ strongly. Moreover, in one dimension, the STS depinning exponent is unphysical ($\zeta_{\text{dep}} \sim 1.25 > 1$), and will probably not be observable in nature. In Fig. 10, we show the structure factor for the model with hard metric constraints as a function of the force, from the statics,
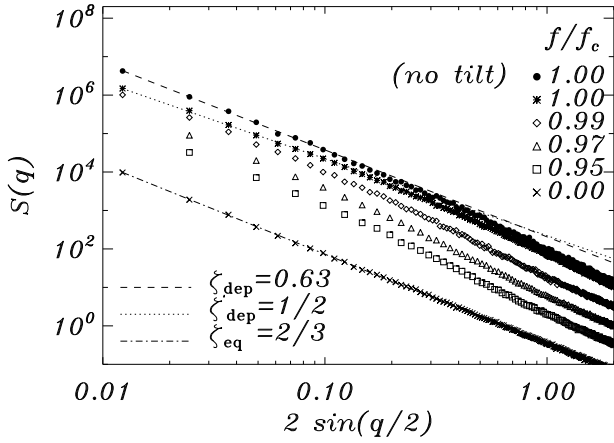
FIG. 11: Steady-state structure factor for a tilted string with hard metric constraint in the Arrhenius limit (averaged over 1000 disorder realizations) for $L = M = 512, 256$. Curves for different forces are shifted for clarity.

FIG. 12: Mean escape barrier U from the dominant configuration for samples $L \times L^{\zeta_{\mathrm{dep}}}$ with $L = 32, 64, 128$ (the line is a guide to the eye).

$f = 0$, to the depinning, $f = f_c$. The small-q region is again consistent with the depinning roughness exponent, and at large-q, we recover once more the equilibrium behavior. However, the collapse of the curves for different values of f/f_c is not possible because the two exponents are now very close in value. The crossover between the two regimes no longer depends on the length scale L_{opt} alone, but also on the microscopic parameters for which the string senses the presence of anharmonic corrections to the elastic energy, that is, when $\overline{(h_{i+1} - h_i)^2} \sim 1$.

In the absence of STS, the roughness exponents at equilibrium and at depinning are very close ($\zeta_{\mathrm{dep}} \sim 0.63$ against $\zeta_{\mathrm{eq}} = 2/3$). However, the physics is very different in the two regimes and reliable signals of the no-STS depinning regime are present when a tilt is applied. A tilt can be realized through a shift $s \cdot L$ imposed on the interface boundary conditions (i.e. $h_L = h_0 + s \cdot L$ and $0 < s < 1$). Following Ref [57] the roughness exponent for a tilted interface will differ from that of an untilted one, and for a tilted string it is expected to be $\zeta_{\mathrm{tilt}} = 0.5$ [58]. In Fig. 11 we show the structure factor for the model with hard metric constraints in presence of a tilt $s = 0.5$. In the statics, $f = 0$, the tilt has no effect. For $f > 0$ we observe that tilted interfaces, at large length scales become less rough than untilted ones, in good agreement with $\zeta_{\mathrm{tilt}} \approx 0.5$. This analysis confirms that in the creep regime the large scale structure of the string is described by deterministic processes belonging to the corresponding depinning universality class of the system, regardless of the violation of the STS symmetry.

B. Barriers

In the Arrhenius limit, the velocity of the interface depends only on the barrier height. Assuming a narrow
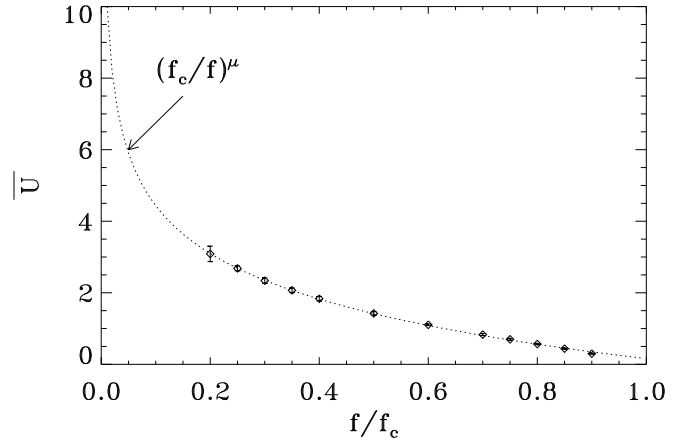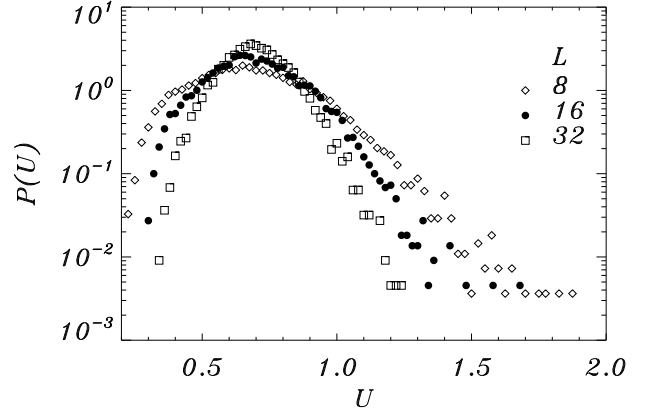

FIG. 13: Distribution of U for 11000 disorder realizations (samples $L \times L^{\zeta_{\mathrm{dep}}}$ with $L = 8, 16, 32$). The width of the distribution decreases with increasing L.

distribution of barriers, we can relate the mean velocity of the interface to the typical barrier $U(f)$:

$$v(f) = L_{\mathrm{opt}}^{\zeta_{\mathrm{eq}}} \left(\frac{L_{\mathrm{relax}}}{L_{\mathrm{opt}}} \right)^{\zeta_{\mathrm{dep}}} e^{-\beta U(f)} \qquad (14)$$

In the creep regime, when f is very small, we have $L_{\mathrm{relax}} \sim L_{\mathrm{opt}}$ and $U(f)$ is given by Eq. (12). The phenomenological expression for the velocity at low forces is the stretched exponential of the creep formula [42, 48, 49, 50, 51]

$$v(f) \sim \exp[-\beta(f_c/f)^\mu]. \qquad (15)$$

Our algorithm yields the escape barrier from the dominant configuration. For a proper scaling [59] of the sample dimensions $L \times L^{\zeta_{\mathrm{dep}}}$, we may identify this barrier
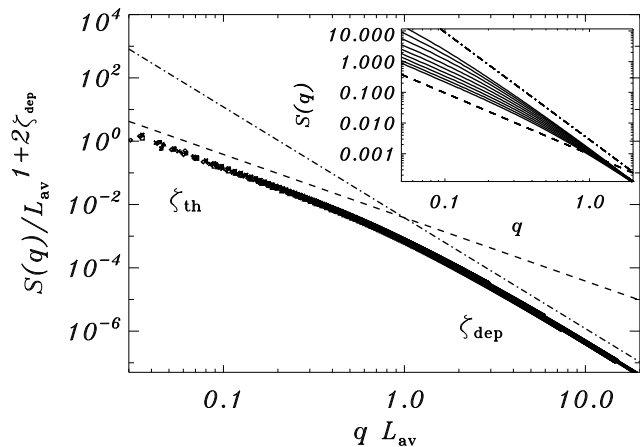
FIG. 14: Finite-temperature Steady-state structure factor from Langevin simulations of an harmonic string of size $(L, M) = (1024, 2048)$. The inset shows $S(q)$ for $T = 0.05$ and $f/f_c = 0.8, 0.85, \dots 1.2$. The crossover length ξ is a fit parameter for the collapse in the main panel.

FIG. 15: ξ as a function of f for different T increasing from the top to the bottom ($T = 0.0025, 0.005, 0.01, 0.025, 0.05, 0.075, 0.1, 0.15, 0.2$).

with the characteristic barrier $U(f)$ and test the phenomenological argument of Eq. (15). In Fig. 12 we see that $U(f)$ increases with decreasing f. This is consistent with the phenomenological arguments leading to Eq. (12), even if we cannot determine the exponent μ, because of the shortcomings of our algorithm at very small driving forces.

In Fig. 13, we show the barrier distribution as a function of the size L for samples scaled properly as $L \times L^{\zeta_{\rm dep}}$. The decay of the distribution for large U appears faster than exponential. Clearly, the distribution becomes narrower as the system size is increased. Extrapolation of these results for an infinite system leads to a well-defined value of $U(f)$, confirming the phenomenological assumption of a typical barrier size.

C. Finite temperature

Our algorithm of Section IV is powerful, but it takes the $T \to 0$ limit before the thermodynamic limit. For a macroscopic physical system, the order of these limits should be interchanged. To confirm that the order of limits does not affect physical properties, we have thus performed Langevin simulations of the equation of motion Eq. (4) at small finite temperatures with parameters $\eta = c = 1$ and with random-bond disorder from a normal distribution interpolated with a cubic spline, as in [60].

In the inset of Fig. 14, we show $S(q)$ for the steady-state motion of the string at $T = 0.05$ for different forces around f_c. Two regimes are always present. They correspond to the depinning at small scales and the flow regime at large scales. The crossover between these regimes corresponds to the correlation length $\xi(f)$ of Fig. 5. In the main panel of Fig. 14 we have collapsed
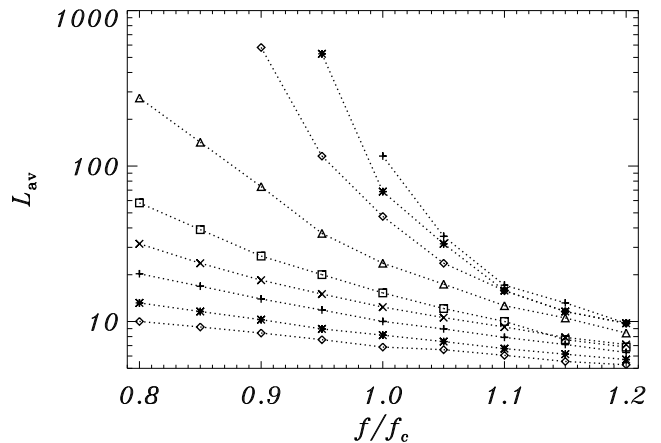
all data at small q by using the scaling $S(q)/S(2\pi/\xi) \sim G(q\xi)$ with a fitting parameter ξ.

The collapse of Fig. 14 provides the correlation length ξ as a function of force and temperature, and we show it in Fig. 15 as a function of the reduced force f/f_c for different T. ξ decreases monotonically with f, and tends to diverge near f_c in the $T \to 0$ limit, showing that ξ is ultimately controlled by the velocity of the string. This behavior is fully consistent with the schematic phase diagram of Fig. 5.

In summary, the Langevin simulations confirm the scenario valid for low-temperature Arrhenius dynamics for finite T. We find no indication of a divergent (or even increasing) correlation length as we approach f_c^-. The main modification at finite T is that ξ diverges at $f = 0$ instead of at f_c, since this divergence is controlled by the vanishing of the steady-state velocity.

D. Deterministic avalanches below f_c

In the previous sections we considered two length scales below threshold, namely the size $L_{\rm opt}$ of the optimal thermal excitation, and the correlation length ξ above which the disorder acts effectively as a thermal-like noise. Both lengths appear in steady-state quantities, such as the structure factor $S(q)$ or the velocity v of the interface.

Another length scale, $L_{\rm relax}$ can be identified as the typical size of the deterministic avalanche that drives the interface from the optimal activated jump of size $L_{\rm opt}$ to the next metastable state.

$L_{\rm relax}$ thus measures the distance between consecutive metastable states. As shown in Fig. 16, $L_{\rm relax} - L_{\rm opt}$ diverges approaching f_c from below, with the characteristic exponent $\nu_{\rm dep}$. However, $L_{\rm relax}$ does not describe steady-state properties below the depinning threshold, and represents no genuine divergent length scale below
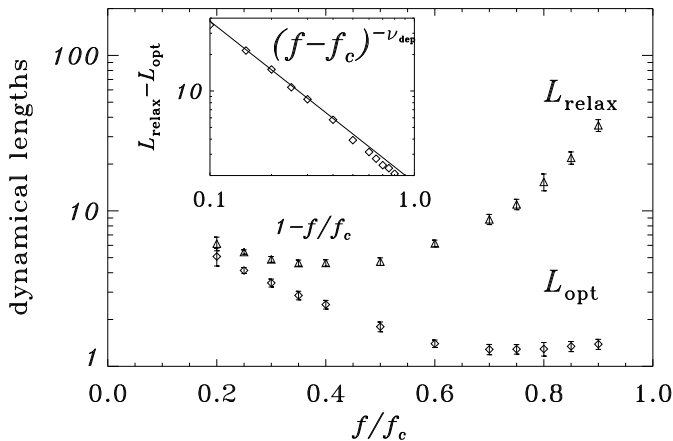
FIG. 16: Behavior of the dynamical length $L_{\rm relax}$. This length diverges with the exponent $\nu_{\rm dep}$ (see inset).

the dynamic phase transition.

A length scale analogous to $L_{\rm relax}$ appears also in the transient dynamics at $T = 0$ for an initially flat configuration which relaxes up to the first pinned metastable state [28, 61]. Here, a crossover separates the large length scales keeping memory of the initial condition from the short length scales characterized by the depinning roughness exponent. This length scale diverges with the same exponent $\nu_{\rm dep}$ as $L_{\rm relax}$. We can identify it with $L_{\rm relax} - L_{\rm opt}$.

VI. DISCUSSION AND CONCLUSIONS

We have studied in this paper the low-temperature dynamics of a driven elastic string in a disordered medium below the depinning threshold. In the (Arrhenius) limit of vanishing temperature, and at large scales, the string behaves as at the critical force ($f = f_c$), and it shows the universal properties of the depinning transition. This result contradicts the quasi-equilibrium picture of the creep motion, which assumes that a small force simply moves the system from one metastable equilibrium state to another, without changing the geometrical properties of these states [49]. It also demonstrates that the analogy of the depinning transition with equilibrium critical phenomena is incomplete. The effect of even a small force ($f \ll f_c$) is in fact more radical: it drives the system away from the equilibrium and into the depinning regime. The equilibrium behavior of the string is restricted to small scales, The crossover between the depinning and the equilibrium regimes takes place at the length scale $L_{\rm opt}$ of the optimal barrier. At the critical force, $L_{\rm opt}$ does not diverge, and it equals the corresponding Larkin length. Lowering the force, $L_{\rm opt}$ increases, diverging in the limit of vanishing force. Our findings are compatible with the FRG predictions [42].

To arrive at these conclusions, we have used a pow-

erful algorithm, which is exact under the condition that the $T \to 0$ limit can be exchanged with the thermodynamic limit. We have also checked its conclusions with conventional Langevin simulations. At finite temperature, a much larger length scale ξ is introduced by the finite velocity of the system. Length scales above ξ are described in terms of the universal fast-flow regime.

The approach of the critical force is not characterized by a divergent length-scale of the steady-state properties. Nevertheless, a divergent length-scale $L_{\rm relax}$ at f_c describes the typical size of the deterministic avalanches that are triggered by the activated events. This deterministic part of the motion does not affect the steady-state geometry and can for example not be identified in snapshot of the line's positions.

The distribution of barriers is narrow and the typical barrier grows with decreasing the drive, in agreement with phenomenological arguments. This shows that the motion is controlled by the typical barriers, yielding a finite steady-state velocity, rather than by rare barriers described by extreme value statistics [62].

We conjecture that our conclusions remain valid for d-dimensional manifolds moving in $d+1$-dimensional space with short-range or long-range elasticity. Moreover, the violation of the statistical tilt symmetry changes only the large-scale geometry according to the change of the universality class at the depinning transition. This may be relevant for the interpretation of creep experiments in thin magnetic films [1, 4], since systems violating STS display a depinning roughness which is very close to the equilibrium one.

Our results may apply to different experiments probing the creep motion of elastic interfaces. We expect that an experimental verification of our results is possible using, for instance, imaging techniques for magnetic [1, 3, 4] or electric [5, 6] domain walls in thin films: $L_{\rm opt}$ could be extracted from the analysis of a spatial correlation function, and $L_{\rm relax}$ could be measured by comparing consecutive (long-lived) metastable states when f is close to f_c, since then $L_{\rm relax}$ controls the distances between successive metastable states. Due to its transient nature $L_{\rm relax}$ could be also measured by transient methods at $T = 0$, where we relax an uncorrelated initial condition until it locks to the first metastable state at a given force.

Steady-state noise measurements (such as acoustic emission noise) below the threshold could also provide an indirect verification of our results. We expect the force dependent barriers shown in Fig. 12 to control the waiting times between events associated with deterministic avalanches of a diverging size $L_{\rm relax}$, translating into large noise peaks. This situation could be realized in ferromagnets [63] or in material failure [64, 65].

APPENDIX A: ALGORITHMIC DETAILS

Our algorithm computes the dominant configuration of an elastic string moving on a two-dimensional discrete $L \times M$ lattice with periodic boundary conditions both in L and in M. The line is described by the variables $h(i)$, giving the displacement of the string on the slice i, with $0 \leq i < L$. The energy of the line is given by

$$E = \sum_i \frac{1}{2}(h(i+1) - h(i))^2 - fh(i) + V(i, h(i)). \quad \text{(A1)}$$

Periodic boundary conditions in M are accounted for by the periodicity of the disorder potential: $V(i, h) = V(i, h + M)$. Besides the harmonic elastic energy (which preserves STS), we also consider a hard metric constraint:

$$|h(i) - h(i-1)| \leq 1 \quad \text{(A2)}$$

which violates STS.

We use elementary moves of the 'variant Monte Carlo' (VMC) algorithm of Ref. [43, 52] which allows for the simultaneous motion of $k+1$ adjacent sites by one lattice spacing if no move of k sites is energetically favorable. This choice of dynamics avoids certain pathologies of the single-site dynamics [43, 52].

For each sample of the disorder potential, the equilibrium ground state [26, 33], the critical depinning force f_c and the associated zero-temperature configuration at f_c [43, 52] can be computed easily.

Below threshold, two kinds of motions are present: the first is deterministic, as defined by the VMC algorithm, and it relaxes each unstable configuration toward a metastable state. The second is the activated dynamics connecting α_k to α_{k+1} through the sequence of VMC moves belonging to the optimal path, which is characterized by the barrier $E_{\text{esc}}[\alpha_k]$.

1. Complete-enumeration scheme

We initialize the dynamics from the equilibrium ground-state, which by its very nature cannot relax through backward moves when the external force is positive. This allows us to restrict our attention to forward moves only (see Appendix A 3). At a given external force, we let the ground state relax toward the metastable configuration α_0. For each transition $\alpha_k \to \alpha_{k+1}$ we build the archive of the visited configurations, β_i, with increasing energy $E[\beta_1] \leq E[\beta_2] \leq E[\beta_3] \leq ....$ A constant E_{cut} is also introduced in order to compute $E_{\text{esc}}[\alpha_k]$. The archive is initialized with a single configuration, $\beta_1 = \alpha_k$, and E_{cut} is set to zero. At each step the configuration β_1 is taken and erased from the archive. Two operations are performed on this configuration. First, we update the maximal barrier

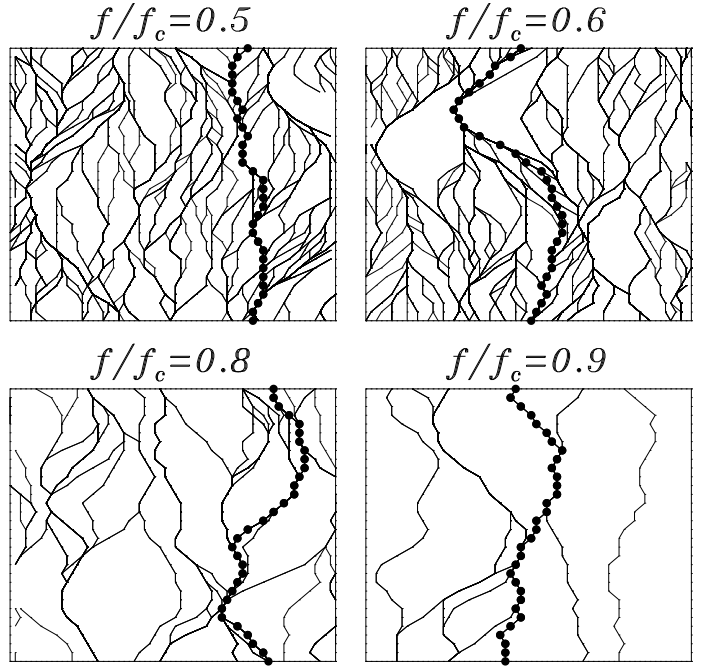$$E_{\text{cut}} = \max(E_{\text{cut}}, E[\beta_1] - E[\alpha_k])$$

FIG. 17: Metastable states of the low-temperature in a $(L, M = 32, 64)$ system, for different forces $f < f_c$. The dominant configuration is emphasized.

Second, we relax β_1 under the VMC dynamics to a configuration β'. All configurations connected to β' by VMC moves are incorporated to the archive. If β' has lower energy than α_k, the construction ends and the barrier E_{cut} as well as the last configuration erased from the archive β_1 and its associated metastable state, β' are output.

We can identify all the quantities defined in the previous sections:

$$\begin{aligned} \alpha_{k+1} &= \beta' \\ E_{\text{esc}}[\alpha_k] &= E_{\text{cut}} \\ L_{\text{opt}}[\alpha_k] &= \sum_i \Theta(h_{\beta_1}(i) - h_{\alpha_k}(i)) \\ L_{\text{relax}}[\alpha_k] &= \sum_i \Theta(h_{\beta'}(i) - h_{\alpha_k}(i)) \end{aligned} \quad \text{(A3)}$$

where $\Theta(x)$ is the step function with the prescription $\Theta(0) = 0$. Let us remark once again that for each realization of disorder we analyze the data corresponding to the configuration with the maximum value of E_{esc}. In Fig. 17 we sketch the output of our algorithm for a small sample at different driving forces.

2. Bound on escape energies

In this section, we show that all configurations between the metastable configurations α_k and α_{k+1} have smaller escape energies than the configuration α_k itself. This assures that the coarse-grained dynamics must pass through the metastable configurations with the largest barrier.
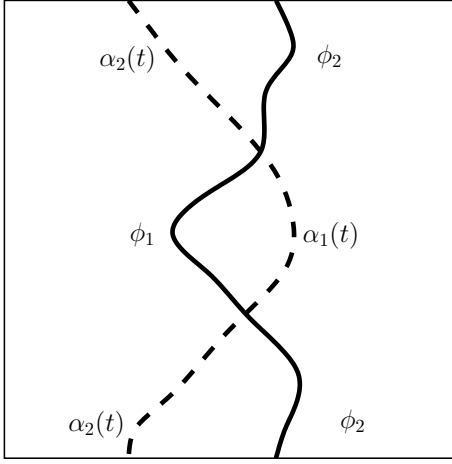
FIG. 18: Decomposition of a configuration $\alpha(t)$ as a sum of $\alpha_1(t)$ and $\alpha_2(t)$, the configuration ϕ by the sum of ϕ_1 and ϕ_2, the configuration $\alpha_\phi(t)$ by the sum of ϕ_1 and $\alpha_2(t)$, and the configuration $\phi_\alpha(t)$ by the sum of $\alpha_1(t)$ and ϕ_2.

Let us consider a configuration α which moves to γ in order to pass through the minimal escape barrier $E_\alpha^{\rm esc}$. We show that any configuration ϕ with $h_\phi(x) \geq h_\alpha(x)$ ($\forall x$) and with an energy barrier $E_\phi^{\rm esc} \geq E_\alpha^{\rm esc}$ satisfies $h_\phi(x) \geq h_\gamma(x)$ ($\forall x$).

We suppose that the property is not true which means that $h_\phi(x) \leq h_\gamma(x)$ for some x. We follow the dynamical evolution of the line $\alpha(t)$ and compare it with the evolution of two sets of configurations. The first one, $\alpha_\phi(t)$, is defined as

$$h_{\alpha_\phi(t)}(x) = \begin{cases} h_\phi(x) & \text{if } h_{\alpha(t)}(x) > h_\phi(x) \\ h_{\alpha(t)}(x) & \text{otherwise} \end{cases} . \quad \text{(A4)}$$

The second one, $\phi_\alpha(t)$, is defined as

$$h_{\phi_\alpha(t)}(x) = \begin{cases} h_\phi(x) & \text{if } h_{\alpha(t)}(x) \leq h_\phi(x) \\ h_{\alpha(t)}(x) & \text{otherwise} \end{cases} . \quad \text{(A5)}$$

We start by comparing $\alpha(t)$ and $\phi_\alpha(t)$. Because of the metastability of ϕ we expect that, initially, $E[\alpha_\phi(t)] \leq E[\alpha(t)]$. However, this situation cannot continue up to $t_{\rm end}$ because, by definition, $\alpha(t)$ is the path which encounters the smallest barrier. We call $\tilde{t}$ the smallest time at which

$$E[\alpha(\tilde{t})] < E[\alpha_\phi(\tilde{t})]. \quad \text{(A6)}$$

Using the decomposition of Fig. 18, for $t = \tilde{t}$, we can write

$$E[\alpha(\tilde{t})] - E[\alpha_\phi(\tilde{t})] = $$
$$E[\alpha_1(\tilde{t})] - E[\phi_1(\tilde{t})] + \Delta E_{\rm el}[\alpha_\phi(\tilde{t}) \to \alpha(\tilde{t})],$$

where the variation of elastic energy is understood as

$$\Delta E_{\rm el}[\alpha_\phi(\tilde{t}) \to \alpha(\tilde{t})] = E_{\rm el}[\alpha_1(\tilde{t}), \alpha_2(\tilde{t})] - E_{\rm el}[\phi_1(\tilde{t}), \alpha_2(\tilde{t})].$$

Let us now compare the energy associated to the configuration $\phi_\alpha(\tilde{t})$ to the energy associated to the metastable state ϕ:

$$E[\phi_\alpha(\tilde{t})] - E[\phi] = E[\alpha_1(\tilde{t})] - E[\phi_1(\tilde{t})] + \Delta E_{\rm el}[\phi \to \phi_\alpha(\tilde{t})].$$

The convexity of the elastic energy assures that

$$\Delta E_{\rm el}[\phi \to \phi_\alpha(\tilde{t})] \leq \Delta E_{\rm el}[\alpha_\phi(\tilde{t}) \to \alpha(\tilde{t})]. \quad \text{(A7)}$$

Using Eq. (A6) we conclude that $E[\phi_\alpha(\tilde{t})] < E[\phi]$. All paths connecting ϕ with $\phi_\alpha(\tilde{t})$ must overcome at least a barrier $E_\phi^{\rm esc}$. This means that there exists a time t^* ($0 < t^* < \tilde{t}$) for which $E[\phi_\alpha(t^*)] - E[\phi] \geq E_\phi^{\rm esc}$. We can use the usual energy decomposition also for the configuration visited at the time t^* (see Fig. 18 for $t = t^*$). The following inequality it is easy to prove:

$$E[\phi_\alpha(t^*)] - E[\phi] \leq E[\alpha(t^*)] - E[\alpha_\phi(t^*)]. \quad \text{(A8)}$$

This implies

$$E[\alpha(t^*)] \geq E[\alpha_\phi(t^*)] + E_\phi^{\rm esc}. \quad \text{(A9)}$$

On the other hand

$$E[\alpha] < E[\alpha_\phi(t^*)]. \quad \text{(A10)}$$

It follows that

$$E[\alpha(t^*)] - E[\alpha] > E_\phi^{\rm Esc.}. \quad \text{(A11)}$$

This contradicts the initial assumption, demonstrating that all configurations between the metastable configurations α_k and α_{k+1} have smaller escape energies than the configuration α_k itself.

3. Effective forward motion

In the present section we prove the following statement: If there is no metastable configuration which lowers the energy of α in the backward direction, the coarse-grained dynamics starting from α will be forever forward-directed. In other words, there exists an escape path starting at α involving only forward motion. This allows us to restrict the search of new configurations, and reduces the complexity of our algorithm. It also allows us to discard the archive of accumulated configurations whenever a new metastable minimum configuration is encountered.

We suppose that the above statement is false by assuming that the configuration γ relaxes towards a configuration ϕ such that, for some x, we have $h_\phi(x) < h_\gamma(x)$. Due to the convexity of the elastic energy we may restrict ourselves to the region where the relaxation is strictly backward and $h_\phi(x) \leq h_\gamma(x)$ for all x. The stability of α with respect to backward movements imposes

$$h_\alpha(x) \leq h_\phi(x) \leq h_\gamma(x) \;\; \forall x. \quad \text{(A12)}$$

The energies associated to these configurations satisfy

$$E[\alpha] > E[\gamma] > E[\phi]. \qquad (A13)$$

We now show that given Eq. (A12) and Eq. (A13), there exists a configuration ϕ_1 for which

$$\begin{aligned} h_\phi(x) \le h_{\phi_1}(x) \le h_\gamma(x) \quad \forall x \\ E[\alpha] < E[\gamma] > E[\phi] > E[\phi_1] \end{aligned}. \qquad (A14)$$

In analogy with Appendix A 2 we can compare the evolution of $\alpha(t)$, $\alpha_\phi(t)$ and $\phi_\alpha(t)$ defined in Eq. (A4) and in Eq. (A5). The configuration ϕ_1 corresponds to $\phi_\alpha(\tilde t)$, where $\tilde t$ is the smallest time at which

$$E[\alpha(\tilde t)] < E[\alpha_\phi(\tilde t)]. \qquad (A15)$$

This construction can be applied to configurations $\phi_2, \phi_3, \ldots$ up to $\phi_n = \gamma$. In this case we have $E[\phi_n] = E[\gamma]$ and the statement is shown to be correct.

APPENDIX B: LONG-RANGE ELASTICITY

For interfaces with long-range interactions, the elastic energy can be written in compact form in the harmonic approximation:

$$E_{\mathrm{el}} = \int d^d q |q|^\alpha h_q h_{-q}. \qquad (B1)$$

Here, the parameter α controls the range of the interactions. The standard short-range interaction corresponds to $\alpha = 2$. The long-range interactions acting on the contact line of a liquid meniscus [23] and on a propagating crack front [24] yield $\alpha = 1$.

We expect the general scenario presented in this paper to remain valid for the long-range case. The numerical values of the universal exponent should depend on the range of the elastic interactions, parameterized by α.

The scaling relations discussed in this paper can be adjusted to the case of general α. From a dimensional analysis of Eq. (B1) we infer the generalization of Eq. (5)

$$\theta = 2\zeta_{\mathrm{eq}} + d - \alpha. \qquad (B2)$$

The four exponents of the depinning transition are still constrained by the hyperscaling relation Eq. (7). In presence of STS, the argument given for $\alpha = 2$ holds and the response function is given by $\partial h(q,t)/\partial \epsilon(q) \sim q^{-\alpha}$. The STS scaling relation writes

$$\nu = \frac{1}{\alpha - \zeta} \qquad (B3)$$

A real-space representation of Eq. (B1) involves fractional derivatives [66].

A discrete version of the force derived from Eq. (B1) is given by [60, 67]

$$f_{\mathrm{el}}[h(i)] = \sum_{j \ne i} \frac{h(j) - h(i)}{|i - j|^{1+\alpha}} \qquad (B4)$$

It presents strong finite-size effects for $\alpha \sim 2$ and all choices $\alpha > 2$ corresponds to the standard Laplacian force. It is more convenient [66] to use the following discretized force

$$f_{\mathrm{el}}[h(i)] = \sum_{j \ne i} A(|i - j|)\,(h(j) - h(i)) \qquad (B5)$$

with

$$A(|i - j|) = \frac{\Gamma(|i - j| - \frac{\alpha}{2})\Gamma(\alpha + 1)}{\pi \Gamma(|i - j| + 1 + \frac{\alpha}{2})} \sin(\frac{\alpha}{2}\pi) \qquad (B6)$$

where $\Gamma(x)$ is the Gamma function. This discretization holds for all $\alpha > 0$, and it is unaffected by slowing down for $\alpha \sim 2$.

[1] S. Lemerle, J. Ferré, C. Chappert, V. Mathet, T. Giamarchi, and P. Le Doussal, Phys. Rev. Lett. **80**, 849 (1998).
[2] M. Yamanouchi, D. Chiba, F. Matsukura, T. Dietl, and H. Ohno, Phys. Rev. Lett. **96**, 096601 (2006).
[3] V. Repain, M. Bauer, J. P. Jamet, J. Ferré, A. Mougin, C. Chappert, and H. Bernas, Europhys. Lett. **68**, 460 (2004).
[4] P. J. Metaxas, J. P. Jamet, A. Mougin, M. Cormier, J. Ferre, V. Baltz, B. Rodmacq, B. Dieny, and R. L. Stamps, Phys. Rev. Lett. **99**, 217208 (2007).
[5] P. Paruch, T. Giamarchi, and J. M. Triscone, Phys. Rev. Lett. **94**, 197601 (2005).
[6] P. Paruch and J. M. Triscone, Appl. Phys. Lett. **88**, 162907 (2006).
[7] S. Moulinet, A. Rosso, W. Krauth, and E. Rolley, Phys. Rev. E **69**, 35103(R) (2004).
[8] L. Ponson, D. Bonamy, and E. Bouchaud, Phys. Rev. Lett. **96**, 35506 (2006).
[9] M. Alava, P. K. V. V. Nukalaz, and S. Zapperi, Adv. Phys. **55**, 349 (2006).
[10] G. Blatter, M. V. Feigel'man, V. B. Geshkenbein, A. I. Larkin, and V. M. Vinokur, Rev. Mod. Phys. **66**, 1125 (1994).
[11] X. Du, G. Li, E. Y. Andrei, M. Greenblatt, and P. Shuk, Nature Physics **3**, 111 (2007).
[12] T. Nattermann and S. Brazovskii, Adv. Phys. **53**, 177 (2004).
[13] T. Giamarchi, in *Quantum phenomena in mesoscopic systems*, edited by I. P. Society (IOS Press, Bologna, 2004), cond-mat/0403531.
[14] D. S. Fisher, Phys. Rev. B **31**, 1396 (1985).

[15] L. W. Chen and M. C. Marchetti, Phys. Rev. B **51**, 6296 (1995).

[16] S. Bustingorry, A. B. Kolton, and T. Giamarchi, Europhys. Lett. **81**, 26005 (2008).

[17] D. Vandembroucq, R. Skoe, and S. Roux, Phys. Rev. E **70**, 051101 (2004).

[18] A. B. Bortz, M. Halos, and J. L. Lebowitz, J. Comp. Phys **17**, 10 (1975).

[19] W. Krauth and O. Pluchery, J. Phys. A **27**, L715 (1994).

[20] W. Krauth, *Statistical Mechanics: Algorithms and Computations* (Oxford University Press, 2006).

[21] A. B. Kolton, A. Rosso, T. Giamarchi, and W. Krauth, Phys. Rev. Lett. **97**, 057001 (2006).

[22] T. Nattermann, J. Phys. C **16**, 4125 (1983).

[23] J. F. Joanny and P. G. de Gennes, J. Chem. Phys. **81**, 552 (1984).

[24] H. Gao and J. R. Rice, J. Appl. Mech. **56**, 828 (1989).

[25] A. I. Larkin and Y. N. Ovchinnikov, J. Low Temp. Phys **34**, 409 (1979).

[26] D. A. Huse and C. L. Henley, Phys. Rev. Lett. **54**, 2708 (1985).

[27] D. S. Fisher, Phys. Rev. Lett. **56**, 1964 (1986).

[28] A. B. Kolton, A. Rosso, E. V. Albano, and T. Giamarchi, Phys. Rev. B **74**, 140201 (2006).

[29] L. H. Tang, M. Kardar, and D. Dhar, Phys. Rev. Lett. **74**, 920 (1995).

[30] M. Kardar, G. Parisi, and Y. Zhang, Phys. Rev. Lett. **56**, 889 (1996).

[31] A. Tanguy and T. Vettorel, Eur. Phys. J. B **38**, 71 (2004).

[32] T. Giamarchi and P. Le Doussal, Phys. Rev. B **52**, 1242 (1995).

[33] M. Kardar, Phys. Rev. Lett. **55**, 2923 (1985).

[34] M. Kardar, Nucl. Phys. B **290**, 582 (1987).

[35] D. S. Fisher and D. S. Huse, Phys. Rev. B **43**, 10728 (1991).

[36] A. B. Kolton, A. Rosso, and T. Giamarchi, Phys. Rev. Lett. **95**, 180604 (2005).

[37] B. Drossel and M. Kardar, Phys. Rev. E **52**, 4841 (1995).

[38] C. Monthus and T. Garel, J. of Phys. A: Math. Gen. **41**, 115002 (2008).

[39] P. Le Doussal, K. J. Wiese, and P. Chauve, Phys. Rev. B **66**, 174201 (2002).

[40] T. Nattermann, S. Stepanow, L. H. Tang, and H. Leschhorn, J. Phys. (Paris) **2**, 1483 (1992).

[41] O. Narayan and D. Fisher, Phys. Rev. B **48**, 7030 (1993).

[42] P. Chauve, T. Giamarchi, and P. Le Doussal, Phys. Rev. B **62**, 6241 (2000).

[43] A. Rosso and W. Krauth, Phys. Rev. Lett. **87**, 187002 (2001).

[44] P. L. Doussal and K. J. Wiese, Phys. Rev. E **67**, 016121 (2003).

[45] L.-H. Tang and H. Leschhorn, Phys. Rev. A **45**, R8309 (1992).

[46] S. V. Buldyrev, A.-L. Barabasi, F. Caserta, S. Havlin, H. E. Stanley, and T. Vicsek, Phys. Rev. A **45**, R8313 (1992).

[47] O. Duemmer and W. Krauth, Phys. Rev. E **71**, 61601 (2005).

[48] A. B. Kolton, A. Rosso, and T. Giamarchi, Phys. Rev. Lett. **94**, 47002 (2005).

[49] L. B. Ioffe and V. M. Vinokur, J. Phys. C **20**, 6149 (1987).

[50] T. Nattermann, Europhys. Lett. **4**, 1241 (1987).

[51] M. Mueller, D. A. Gorokhov, and G. Blatter, Phys. Rev. B **63**, 184305 (2001).

[52] A. Rosso and W. Krauth, Phys. Rev. B **65**, 12202 (2002).

[53] A. A. Middleton, Phys. Rev. Lett. **68**, 671 (1992).

[54] F. Igloi and C. Monthus, Phys. Rep. **412**, 277 (2005).

[55] B. Derrida, J. Stat. Phys. **31**, 433 (1983).

[56] P. Le Doussal and V. M. Vinokur, Physica C **254**, 63 (1995).

[57] T. Goodman and S. Teitel, Phys. Rev. E **69**, 062105 (2004).

[58] M. Kardar, Phys. Rep. **301**, 85 (1998).

[59] C. Bolech and A. Rosso, Phys. Rev. Lett. **93**, 125701 (2004).

[60] A. Rosso and W. Krauth, Phys. Rev. E **65**, 025101R (2002).

[61] H. Ji and M. O. Robbins, Phys. Rev. A **44**, 2538 (1991).

[62] C. Monthus and T. Garel, Phys. Rev. E **78**, 041133 (2008).

[63] J. P. Sethna, K. A. Dahmen, and C. R. Myers, Nature (London) **410**, 242 (2001).

[64] D. Bonamy, S. Santucci, and L. Ponson, Phys. Rev. Lett. **101**, 045501 (2008).

[65] J. Koivisto, J. Rosti, and M. J. Alava, Phys. Rev. Lett. **99**, 145504 (2007).

[66] A. Zoia, A. Rosso, and M. Kardar, Phys. Rev. E **76**, 021116 (2007).

[67] A. Tanguy, M. Gounelle, and S. Roux, Phys. Rev. E **58**, 1577 (1998).